



## NRC Publications Archive Archives des publications du CNRC

### Development and validation of a stabilized immersed boundary CFD model for freezing and melting with natural convection

Blais, Bruno; Ilinca, Florin

This publication could be one of several versions: author's original, accepted manuscript or the publisher's version. / La version de cette publication peut être l'une des suivantes : la version prépublication de l'auteur, la version acceptée du manuscrit ou la version de l'éditeur.

For the publisher's version, please access the DOI link below. / Pour consulter la version de l'éditeur, utilisez le lien DOI ci-dessous.

#### **Publisher's version / Version de l'éditeur:**

<https://doi.org/10.1016/j.compfluid.2018.03.037>

*Computers & Fluids*, 2018-03-12

#### **NRC Publications Record / Notice d'Archives des publications de CNRC:**

<https://nrc-publications.canada.ca/eng/view/object/?id=cb39dce2-dc27-49c6-b437-295bfd65f3f1>

<https://publications-cnrc.canada.ca/fra/voir/objet/?id=cb39dce2-dc27-49c6-b437-295bfd65f3f1>

Access and use of this website and the material on it are subject to the Terms and Conditions set forth at

<https://nrc-publications.canada.ca/eng/copyright>

READ THESE TERMS AND CONDITIONS CAREFULLY BEFORE USING THIS WEBSITE.

L'accès à ce site Web et l'utilisation de son contenu sont assujettis aux conditions présentées dans le site

<https://publications-cnrc.canada.ca/fra/droits>

LISEZ CES CONDITIONS ATTENTIVEMENT AVANT D'UTILISER CE SITE WEB.

#### **Questions?** Contact the NRC Publications Archive team at

PublicationsArchive-ArchivesPublications@nrc-cnrc.gc.ca. If you wish to email the authors directly, please see the first page of the publication for their contact information.

**Vous avez des questions?** Nous pouvons vous aider. Pour communiquer directement avec un auteur, consultez la première page de la revue dans laquelle son article a été publié afin de trouver ses coordonnées. Si vous n'arrivez pas à les repérer, communiquez avec nous à PublicationsArchive-ArchivesPublications@nrc-cnrc.gc.ca.



# Development and Validation of a Stabilized Immersed Boundary CFD Model for Freezing and Melting with Natural Convection

Bruno Blais<sup>a,\*</sup>, Florin Ilinca<sup>a</sup>

<sup>a</sup>*National Research Council (NRC) Canada, 75 De Mortagne Boul., Boucherville, QC, Canada, J4B 6Y4*

---

## Abstract

Numerous processes in the automotive, additive manufacturing or energy storage industries require an accurate prediction of the solidification (freezing) and melting (thawing) dynamics of substances, whether they be pure or blends of components. The numerical modelling of such phase change is highly complex because it includes sharp moving interfaces and strong discontinuities in the materials properties. This complexity is often exacerbated by the occurrence of natural convection, which induces a strong coupling between the motion of the melted fluid and the position of the solid-liquid interface. This leads to strongly coupled non-linear stiff thermo-fluid problems which have to be solved in complex geometries.

In this work, we introduce two novel stabilized finite element model to predict the phase change with natural convection. The first model uses a more classical viscosity approach to impose stasis in the solidified region whereas the second one is based on an immersed boundary formulation to accurately describe the solid-fluid interface.

The efficiency of the stabilized approach is first demonstrated by studying the Stefan problem. The two approaches to impose stasis are then compared using 2D test cases before they are both used to study melting in a rectangular

---

\*Corresponding author

Email address: `bruno.blais@cnrc-nrc.gc.ca` (Bruno Blais)

(2D) and prismatic (3D) cavity. Significant differences are observed in the flow profiles and the solid-liquid interface between the 2D and the 3D simulations.

*Keywords:* Multiphase flows; Melting and Freezing; Selective Catalytic Reduction (SCR); Computational Fluid Dynamics; Finite Element Method; Immersed Boundary Method.

---

## 1. Introduction

The modelling of solidification and melting (or thawing) is a challenging topic which had initially been studied extensively in the 80's and 90's for its application in metallurgical processes such as casting in order to predict the crystal growth structure and the ensuing metallurgic properties [1, 2, 3, 4]. Since then, it has garnered continuous large interest for energy applications such as latent heat storage [5, 6, 7, 8, 9, 10]. In this latter application, the interest has lied more in predicting accurately the melting or freezing rate and the overall heat storage instead of the precise position of the solid-liquid interface.

Other recent applications require an accurate prediction of the position of the melting and solidification interface. An example lies in the storage of Ad-Blue, a urea-water solution which is used for the Selective Catalytic Reduction (SCR) of the exhaust gas of diesel engines [11, 12, 13]. The implementation of this technology, which has the potential to greatly reduce nitrogen oxides ( $\text{NO}_x$ ) emissions, faces considerable challenges in colder regions of the world since Ad-Blue freezes and expands around  $-11^\circ\text{C}$ . This has two effects. First, the tanks must be able to handle freezing of the fluid without endangering the structure of the vessel, which could lead to leakage or worse, total breakage. Considering the complex shape that such reservoir can take, this requires an accurate prediction of the solidification front in order to prevent the occurrence of liquid entrapment in solidified Adblue. Such entrapment leads to the generation of a high pressure zone which could distort or break components. This has to be predictable while taking into account various factors which may alter the freezing dynamics, such as the parking angle of the vehicle. Secondly, the tank must house components

that can thaw a sufficient amount of AdBlue using minimal energy so that the system can operate even if the majority of the tank remain frozen. Thus, it is important to develop robust numerical models that can simulate freezing and thawing while predicting the position of the interface with great accuracy in order to ensure adequate design and operation of SCR components.

A second application lies in laser powder-bed fusion additive manufacturing. In this type of process, a laser is used to melt metal powder, creating a melted pool of liquid which then solidifies, ensuring buildup of the desired geometry [14, 15]. For such processes, accurate prediction of the solid-liquid interface and the flow dynamics are critical.

From a physical and mathematical point of view, the modelling of phase change (i.e. melting or solidification) is complex since they lead to sharp moving non-linear interfaces, an issue that may be exacerbated by the occurrence of natural convection. When the flow is at high Rayleigh number, natural convection can have a considerable influence on the freezing or melting processes since the motion of the fluid alters the temperature gradient felt at the solidified interface. We recall the definition of the Rayleigh number :

$$Ra = \frac{\rho^2 \beta g (T_w - T_s) L^3}{k \mu} \quad (1)$$

with  $\rho$  the density of the fluid,  $\beta$  its linear coefficient of expansion,  $g$  the gravity,  $T_w$  the wall temperature,  $T_s$  the melting point temperature,  $k$  the thermal conductivity,  $\mu$  the dynamic viscosity and  $L$  the characteristic dimension of the liquid volume. Models for freezing and melting become inherently complex due to the coupling between the solid-liquid discontinuity, the natural convection and the non-linear variations of the physical properties of the material (such as the thermal conductivity) [16]. Consequently, the velocity and the energy equation become tightly coupled. However, the phase change can occur on a very slow time scale compared to the convective or conductive one. This separation of time scale is in part characterized by the Stefan numbers for melting ( $St_m$ ) and

solidification ( $St_s$ ):

$$St_m = \frac{c_p (T_w - T_m)}{h_l} \quad (2)$$

$$St_s = \frac{c_p (T_m - T_c)}{h_l} \quad (3)$$

with  $c_p$  the specific heat,  $h_l$  the latent heat,  $T_m$  is the melting (or solidification) temperature and  $T_w$  or  $T_c$  is the temperature of the heating or cooling wall respectively. This must be taken into account when designing numerical methods. It can, for instance, render direct explicit approach prohibitively expensive due to the long physical time that must be simulated.

Numerous models have been developed to model solidification and melting. The models can be distinguished by two traits: the manner in which the latent heat due to the phase change is modeled and the strategy used to impose stasis within the solidified fluid. Generally, the phase change is taken into account by introducing a solidification interval ( $\Delta T = T_l - T_s$ , sometimes referred to as mushy region) over which the contribution of the latent heat is introduced either via a modified specific heat [17] or a volumetric source term [11]. To impose the stasis of the solidified region, Darcy penalization (using velocity), brinkman penalization (using velocity and viscosity), viscous penalization (via a rheological model) or a direct imposition of Dirichlet boundary condition [18] are used. We refer the reader to the work of Angot *et al.* [19] or Blais *et al.* [20] for an analysis of penalization approaches and their consequences on accuracy and robustness.

Many of these strategies (or combinations of strategies) them have been developed in the context of more classical methods such as the finite element (FEM) [17, 18] or finite volume (FVM) approaches [11, 17, 21, 12]. They have also been used in the context of the Lattice Boltzmann method (LBM) with two distinct sets of populations for the velocity and the temperature [22, 23, 24]. In these cases, stasis in the solidified region was imposed either via a viscosity model [22] or a probabilistic porous media approach [23, 24]. However, we recall that the LBM is an explicit method and uses a diffusive time scaling ( $\Delta t \propto \Delta x^2$ ).

Therefore the treatment of cases where there is a sharp separation between the time scale of conduction, convection and melting (esp. for low Stefan number) can be computationally expensive due to the large number of iterations required.

The goal of the present work is to design an implicit 3D finite element model for phase change with natural convection. This requires a formulation for which the phase change can be taken into account in a robust implicit manner without requiring under-relaxation of the non-linear solver as used for instance by Ogoh and Groulx [25]. This will allow the simulation of the full melting and solidification problem while minimizing the issues related to the sharp time scale differences between conduction/convection and phase change. Furthermore, we wish to be able to model phase change of pure and well as non-pure substances and as such, the influence of the solidification interval on the dynamics should be well characterized and, for the case of pure substance, be minimized. As such, the influence of the solidification interval will be investigated therein this work

We present two novel stabilized implicit finite element model for phase changes with natural convection. These model differ by the approach used to impose stasis of the solidified material. In the first model the stasis of the fluid is enforced by using a viscous penalization of the momentum equation. The second approach uses a conformal decomposition to reconstruct the solid-liquid interface within the elements. Thus an immersed boundary condition can be used to impose no-slip on the surface of the solidified material. This decomposition is also used for the energy equation to ensure conformity of the convection terms with the immersed interface.

The approaches to resolve the phase change are first verified on the classical Stefan test case. The role of stabilization to improve the stability and robustness of the model is discussed. The influence of the model parameters on the stability and the accuracy of the model as well as on the thickness of the phase change interval is established using mesh refinement analysis. The accuracy of the strategies used to impose stasis are compared via order of convergence analysis. The model is then validated by studying the melting of solidified liquid

in a rectangular (2D) and prismatic (3D) cavity heated up by its lateral wall. Comparison with the literature shows that the models are able to reproduce melting front instabilities at high Rayleigh number and the relative accuracy of the models are compared. Future work possibilities deriving from this model, such the modelling of phase change of substances with different solid and liquid densities, are discussed as concluding remarks.

## 2. Model Formulation

The incompressible Navier-Stokes equations describing the momentum and mass conservation with the Boussinesq approximation are used in the present work [26]

$$\nabla \cdot \mathbf{u} = 0 \quad (4)$$

$$\rho \frac{\partial \mathbf{u}}{\partial t} + \rho (\mathbf{u} \cdot \nabla) \mathbf{u} = -\nabla p + \nabla \cdot \boldsymbol{\tau} + \rho \beta \mathbf{g} (T - T_r) \quad (5)$$

where  $\rho$  is the fluid density evaluated at a reference temperature,  $\mathbf{u}$  is the velocity,  $\beta$  is the linear coefficient of thermal expansion,  $T$  is the fluid temperature and  $T_r$  is a reference temperature around which the density variation is linearized. The deviatoric stress tensor for an incompressible fluid,  $\boldsymbol{\tau}$ , can be expressed as a function of the velocity gradient:

$$\boldsymbol{\tau} = (\mu (\nabla \mathbf{u} + \nabla \mathbf{u}^T)) \quad (6)$$

The energy equation is [26] :

$$\rho \frac{\partial}{\partial t} (c_p T) + \rho \mathbf{u} \cdot \nabla (c_p T) = \nabla \cdot (\lambda \nabla T) \quad (7)$$

where  $c_p$  is the specific heat,  $T$  the temperature and  $\lambda$  the thermal conductivity.

In order to correctly account for the energy balance during phase change we compute the specific heat based on the change in enthalpy as :

$$c_p = \frac{H(T) - H(T_0)}{T - T_0} \quad (8)$$

where  $H$  is the temperature dependent enthalpy,  $T$  is the temperature at current time step and  $T_0$  is the temperature at the previous time step. The enthalpy of the fluid,  $H$ , is computed from :

$$H = H_0 + \int_{T_0}^T c_p^*(T^*) dT^* \quad (9)$$

where the specific heat  $c_p^*$  is defined as :

$$c_p^*(T) = \begin{cases} c_{p,s} & \forall T < T_s \\ \frac{c_{p,s} + c_{p,l}}{2} + \frac{h_l}{T_l - T_s} & \forall T \in [T_s, T_l] \\ c_{p,l} & \forall T > T_l \end{cases} \quad (10)$$

where indices  $s$  and  $l$  refer to the solid and liquid state values respectively.

The phase transition (or mushy) interval,  $\Delta T = T_s - T_l$ , controls the temperature interval over which the phase change occurs. For pure substances, in which the phase change occurs at a single temperature,  $\Delta T$  can be seen as numerical parameter to relax the phase transition. However, blended substances, such as Adblue or metal alloys, can solidify or melt over a relatively important temperature range ( $0.5^\circ C$  to  $1^\circ C$ ). In this latter case,  $\Delta T$  should represent the physical phase transition interval.

### 2.1. Finite Element Formulation for the Navier-Stokes equation

In this work, a GLS (Galerkin Least-Squares) formulation is used with continuous linear interpolants for the velocity, the pressure and the temperature. A first order implicit Euler scheme is used for the time derivative. The ensuing weak form for the Navier-Stokes equation are:

$$\begin{aligned} & \int_{\Omega} \rho \left( \frac{\mathbf{u} - \mathbf{u}_0}{\Delta t} + \mathbf{u} \cdot \nabla \mathbf{u} \right) N_i^u d\Omega - \int_{\Omega} p \nabla N_i^u d\Omega + \\ & \int_{\Omega} \mu (\nabla \mathbf{u} + \nabla \mathbf{u}^T) \cdot \nabla N_i^u d\Omega - \int_{\Omega} \rho \beta \mathbf{g} (T - T_r) N_i^u d\Omega + \\ & \sum_K \int_{\Omega_K} \left[ \rho \left( \frac{\mathbf{u} - \mathbf{u}_0}{\Delta t} + \mathbf{u} \cdot \nabla \mathbf{u} \right) + \nabla p - \nabla \cdot [\mu (\nabla \mathbf{u} + \nabla \mathbf{u}^T)] - \rho \beta \mathbf{g} (T - T_r) \right] \\ & \tau_s \mathbf{u} \cdot \nabla N_i^u d\Omega_K = \int_{\Gamma} (\boldsymbol{\tau} \cdot \hat{\mathbf{n}} - p \hat{\mathbf{n}}) N_i^u d\Gamma \end{aligned} \quad (11)$$



$$\begin{aligned}
& \int_{\Omega} \nabla \cdot \mathbf{u} N_i^p d\Omega + \\
& \sum_K \int_{\Omega_K} \left[ \rho \left( \frac{\mathbf{u} - \mathbf{u}_0}{\Delta t} + \mathbf{u} \cdot \nabla \mathbf{u} \right) + \nabla p - \nabla \cdot [\mu (\nabla \mathbf{u} + \nabla \mathbf{u}^T)] - \rho \beta \mathbf{g} (T - T_r) \right] \\
& \tau_s \cdot \nabla N_i^p d\Omega_K = 0
\end{aligned} \tag{12}$$

where  $\mathbf{u}$  and  $p$  are the velocity and pressure solution at the current time step  $t_n$ ,  $\mathbf{u}_0$  is the solution at the previous time step  $t_{n-1}$  and  $\Delta t = t_n - t_{n-1}$  is the time step.  $N_i^u$  and  $N_i^p$  are the continuous, piecewise linear test functions related to the velocity and the pressure respectively. The index  $K$  refers to the element. The first four integrals in the left hand side of 11 and the first integral in the left hand side of 12 correspond to the classical Galerkin formulation whereas the integrals over the element interior are the GLS stabilization terms. The stabilization parameter  $\tau_s$  is computed as [27, 28]:

$$\tau_s = \left[ \left( \frac{2\rho |\mathbf{u}|}{h_K} \right) + \left( \frac{4\mu}{m_K h_K^2} \right)^2 \right]^{-1/2} \tag{13}$$

where  $h_K$  is the size of the element  $K$  (the diameter of the smallest inscribed sphere) and  $m_K$  is a coefficient set to 1/3 for linear elements [27, 29].

## 2.2. SUPG/GGLS stabilized formulation for the energy equation

A SUPG/GGLS formulation of the energy equation is used:

$$\begin{aligned}
& \int_{\Omega} \rho c_p \left( \frac{T - T_0}{\Delta t} + \mathbf{u} \cdot \nabla T \right) N_i^T d\Omega + \int_{\Omega} \lambda \nabla T \cdot \nabla N_i^T d\Omega \\
& + \sum_K \int_{\Omega_K} \left[ \left( \frac{T - T_0}{\Delta t} + \mathbf{u} \cdot \nabla T \right) - \nabla \cdot (\lambda \nabla T) \right] \tau_T (\mathbf{u} \cdot \nabla N_i^T) d\Omega_K \\
& + \sum_K \int_{\Omega_K} \tau_{\nabla} \lambda \nabla \left( \rho c_p \frac{T - T_0}{\Delta t} \right) \cdot \nabla N_i^T d\Omega_K \\
& = - \int_{\Gamma_c} h_c (T - T_c) N_i^T d\Gamma
\end{aligned} \tag{14}$$

where  $T$  is the solution at the current time step  $t_n$ ,  $T_0$  is the solution at the previous time step  $t_{n-1}$  and  $N_i^T$  are the continuous, piecewise linear test functions associated to the temperature equations. The first two integrals in the

left hand side of equation (14) correspond to the Galerkin formulation, the integrals over the elements interior in the third term are the SUPG stabilization and the integrals over the elements interior in the fourth term are the GGLS stabilization. SUPG is used to stabilize the finite element formulation in the presence of important advective terms (high Reynolds number flow) and GGLS is a stabilized method dealing with sharp gradients in the solution [30]. The SUPG stabilization parameter is computed for element  $K$  as [27]:

$$\tau_T = \left[ \left( \frac{2\rho c_p |\mathbf{u}|}{h_K} \right)^2 + \left( \frac{4\lambda}{m_k h_K^2} \right)^2 \right]^{-1/2} \quad (15)$$

The GGLS stabilitation parameter  $\tau_\nabla$  is computed as [30]:

$$\tau_\nabla = \frac{h_K^2}{6\lambda} \bar{\xi}, \quad (16)$$

where

$$\bar{\xi} = \frac{\cosh(\sqrt{6\alpha}) + 2}{\cosh(\sqrt{6\alpha}) - 1} - \frac{1}{\alpha}, \quad (17)$$

$$\alpha = \frac{(\rho c_p / \Delta t) h_K^2}{6\lambda}, \quad (18)$$

The dimensionless parameter  $\bar{\xi}$  tends towards to unity for very large values of  $\alpha$  and to 1/2 for  $\alpha$  much smaller than the unity.

### 2.3. Stasis imposition

Two strategies are considered in the present work to impose the stasis ( $\mathbf{u} = 0$ ) in the solidified region: a viscous penalization (henceforth referred to as  $\mu$ -Penalization) via rheological model and an Immersed Boundary-Body Conformal Enrichment approach (henceforth referred to as IB).

#### 2.3.1. Viscous penalization - $\mu$ -Penalization

In the viscous penalization approach, a rheological model in which the viscosity depends on the fraction of solidified material  $\phi$  is introduced. The solid

fraction is directly related to the temperature via the relation :

$$\phi = \begin{cases} 1 & \forall T < T_s \\ \frac{T_l - T}{T_l - T_s} & \forall T \in [T_s, T_l] \\ 0 & \forall T > T_l \end{cases} \quad (19)$$

Aus der Wiesche *et al.* [11] proposed a semi-empirical viscosity model which is very similar to the Kriger-Dougherty model for solid suspension:

$$\mu = \begin{cases} \mu_s & \forall T < T_s \\ \min \left( \mu_s, \mu_l \left( 1 - \frac{\phi}{\phi_c} \right)^n \right) & \forall T \in [T_s, T_l] \\ \mu_l & \forall T > T_l \end{cases} \quad (20)$$

where  $\mu_l$  is the viscosity of the liquid while  $\phi_c$  and  $n$  are empirical parameters which correspond respectively to a critical solid fraction and a thickening exponent. The solid viscosity,  $\mu_s$ , is a numerical parameter to impose stasis. Preferably,  $\mu_s$  should be chosen to be sufficiently large in order to ensure no advection of solidified material in the bulk of the flow, but not too large in order not to degrade too significantly the condition number of the global system matrix.

### 2.3.2. Immersed Boundary-Body Conformal Enrichment - IB

The Immersed Boundary-Body Conformal Enrichment method introduced by Ilinca and Héty [31, 32, 33, 34, 35, 36, 37] is extended in the present work to natural convection flow in the presence of phase change. Instead of using a penalization technique to approximate the no-flow behavior in the solid region, the IB method uses a local enrichment of the velocity interpolation space such as to be able to represent accurately the solid-liquid interface when it lies within elements. The procedure was described in details in [31, 32]. This method was previously extended to study natural convection [36] and conjugated heat transfer [37], but only in static configurations.

In the case of solid geometries, the position of the interface can be described using an analytical signed distance function. The case of phase change studied

in the present work is significantly different because of the motion of interface is controlled by the energy equation. Thus, the position of the interface is described using the nodal temperature values as well as a critical temperature value which is generally equal to the liquidus temperature  $T_l$ .

Elements which are cut by the fluid/solid interface are decomposed into sub-elements which are either entirely in the fluid or entirely in the solid regions. Then, flow equations are solved in the entire fluid region (i.e. including fluid sub-elements) and the velocity at interface nodes is imposed as a boundary condition, while the pressure degrees of freedom at interface nodes are eliminated at element level by static condensation.

Since the local enrichment of the velocity and pressure interpolation space is condensed at the element level, these degrees of freedom are not kept globally and cannot be used straightforwardly. Consequently, a special procedure must be carried out to calculate the convection terms of Eq. (14). For each of the element which contain an interface, the interpolation space for velocity is locally enriched using the nodal values as well as the value at the interface which is known due to the no-slip boundary condition. This does not lead to any additional degree of freedoms, as the velocity are knowns at the time of the calculation, but this alters the integration rules by adding gauss points and altering their position as a function of the interface position. Thus, the integration rule for the convection term can be changed to take into account the enriched velocity space without altering the underlying mesh.

We have found that this local enrichment of the velocity interpolation space for the energy equation was necessary, otherwise strong convection of solidified material would occur which lead to results which were non-physical.

#### 2.4. Error calculations

For the three verification test case investigated in this article, the methods are compared using the  $\mathcal{L}^2$  norm of the error which is defined as :

$$\|e(\xi)\|_2 = \left( \sum_{ie}^{N_e} \int_{\Omega_K} (\xi - \xi_a)^2 d\Omega_K \right)^{\frac{1}{2}} \quad (21)$$

where  $\|e(\xi)\|_2$  is the  $\mathcal{L}^2$  norm of the error for  $\xi$ ,  $K$  is the element number,  $\Omega_K$  is the element volume and  $\xi$  and  $\xi_a$  are respectively the numerical solution and analytical solution for a variable (i.e temperature, velocity). The integration over each element (tetrahedral in our case) is carried out using the same Gauss integration rule used in the element integration of the finite element formulation.

### 2.5. Implementation of the model

Both the  $\mu$ -Penalization and the *IB* approaches were implemented in our in-house software DFEM. This software allows memory efficient MPI domain decomposition where each of the processes are aware of their local elements and the surrounding ghost nodes. As such, large problems can be solved without necessitating a large amount of memory since the value of the unknowns are only stored for the processes in which they belong.

In DFEM, the Navier-Stokes equation with Boussinesq hypothesis (4) and the energy equation (7) are solved in a decoupled fashion and global iterations are carried out within each time-step to ensure convergence of the two-way coupling between the two equations. We have found that few global iterations (two to three) were required for convergence in transient analysis. Considering the stiffness of the energy equation due to the phase change, we believe this approach is more robust and faster than a monolithic resolution.

This software was verified using the method of manufactured solutions notably for flows and temperature (or enthalpy) profiles for which non-trivial two-way coupling between (4) and (7) was ensured. We refer to [38, 39] for an extensive presentation of the method of manufactured solutions and to Blais and Bertrand [40] for the procedure used to implement it automatically using Python.

## 3. Verification

### 3.1. Stefan problem

The Stefan problem describes the melting or the solidification of a pure substance by conduction in a 1D semi-infinite domain. This classical problem,

extensively described in the literature [11], is often used as the core test case to establish the accuracy and the robustness of numerical scheme for phase change. Although it is established for a semi-infinite domain, it can be solved on a finite domain provided that it is sufficiently long. In this case, insulation (Neumann) boundary condition are applied at the end. This problem is illustrated in Figure 1.



Figure 1: In the Stefan test case, a solidified fluid is allowed to thaw, which in turns displaces the solid-liquid interface.

The solution for the temperature in the liquid is given by:

$$\frac{T(x, t) - T_w}{T_s - T_w} = \frac{\operatorname{erf}\left(\frac{x\sqrt{\frac{\Delta}{\rho}}}{2}\right)}{\operatorname{erf}(\beta)} \quad (22)$$

where  $T_w$  is the wall temperature and  $T_s$  is the melting (or solidification) point of a pure substance. The parameter  $\beta$  is obtained by solving the non-linear algebraic equation:

$$\beta \exp^{\beta^2} \operatorname{erf}(\beta) = \frac{Ste}{\sqrt{\pi}} \quad (23)$$

In the present work this equation is solved using the SciPy package and Python [41]. The displacement of the melting front (the dashed lined in Figure 1) is:

$$\delta(t) = 2\beta\sqrt{\alpha_l t} \quad (24)$$

with  $\alpha_l = \frac{\lambda_l}{\rho_l C_{pl}}$  the diffusivity coefficient in the liquid phase and  $\delta(t)$  the melting front displacement.

Although simple, this problem can be challenging to solve numerically because of the sharp impact of the phase change on the specific heat within the solidification interval. Even if this problem is inherently a 1D problem, we analyse it in 3D by generating structured hexahedral meshes on a  $[0, 0, 0] \times [1, 0.1, 0.1]$

domain. The number of nodes in the  $y$  and  $z$  directions is kept constant at 6 (for 5 intervals), but it is adjusted from 101 to 1001 in the  $x$  direction which represents the direction in which the heat transfer occurs (3636 to 36036 total nodes or DOF). Finally, these hexahedrons are each divided into 5 tetrahedron. This only changes the number of elements, but does not alter the number of nodes. In what follow,  $\Delta x$  is defined as the distance in the  $x$  direction between each nodes.

Figure 2 shows a typical result for  $St_l = 0.01$ ,  $\alpha_l = 1$ ,  $\Delta x = 0.01$  and  $\Delta T = 0.01$  with GGLS stabilization. It can be seen that even for a relatively coarse mesh, a very sharp interface can be captured between the liquid and solid phase. Indeed, the smoothing of the interface due to the solidification interval is barely perceivable for this case.

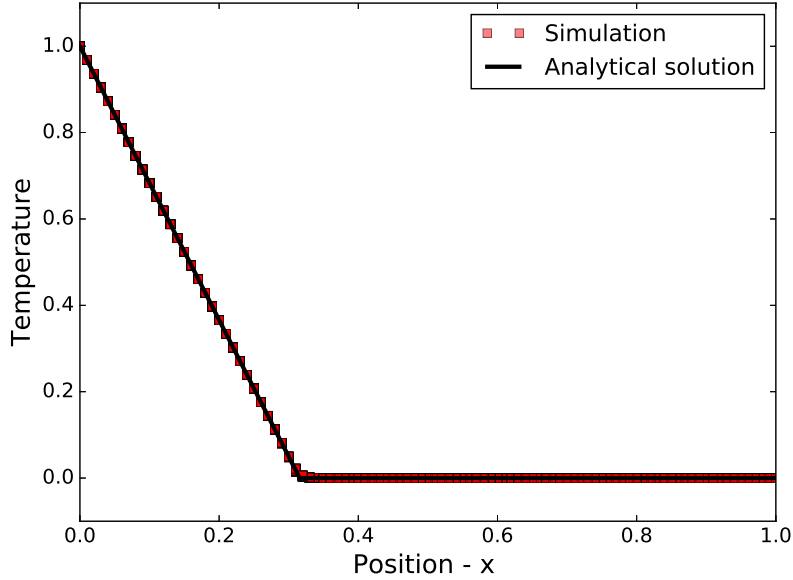


Figure 2: Temperature profile for the Stefan problem with  $St_l = 0.01$ ,  $\alpha_l = 1$ ,  $\Delta x = 0.01$  and  $\Delta T = 0.01$ .

We then investigate the influence of the phase change interval  $\Delta T = T_l - T_s$  as well as the mesh size on the error of the numerical solution for both

the stabilized and non-stabilized scheme. All simulations are carried out using a constant ratio between the time step and the mesh size such that  $\Delta x \propto \Delta t$ . Furthermore, the final time (5s) is chosen so that the Neumann boundary condition used to model the semi-infinite domain does not alter the solution. For the coarser mesh ( $\Delta x = 0.01$ ), 100 time steps are used to simulate 5s. Consequently, 200 time steps are used for  $\Delta x = 0.005$ , 400 for  $\Delta x = 0.0025$  and so on and so forth.

We note that the analytical solution for the Stefan problem is defined for a pure substance. Consequently, on an uniform mesh, the  $\mathcal{L}^2$  norm of the error measured in our analysis will be due to two component:

$$\|e(T)\|_2 \propto h_e^2 + g(\Delta T) \quad (25)$$

where  $h_e$  is the element size and  $g(\Delta T)$  is an unknown function. The goal of this analysis is to assess the relative importance of these two errors and to demonstrate that the scheme is coherent and that, as  $h_e$  and  $\Delta T$  go towards zero, the error also goes to zero. Figure 3 and 4 present the  $\mathcal{L}^2$  norm of the error for the temperature for the non-stablized and the GGLS stabilized approach. Clearly, the value of the solidification interval  $\Delta T$  has the highest impact on the norm of the error. It can be seen that for higher values of  $\Delta T$ , the solutions is barely affected by the mesh size. The discretization error is negligible in front of the solidification interval error and the solidification interval is sufficiently large such that it is smoothly represented on all meshes. This is true for both the stablized and non-stablized cases.

For coarse meshes ( $\Delta x = 0.01$ ) in both cases (Figure 3 and Figure 4), decreasing the value of  $\Delta T$  lowers the error up until a certain value of the solidification interval ( $\Delta T = 0.02$ ) for the non-stablized and  $\Delta T = 0.01$  for the stabilized). This decrease in error is due to a sharpening of the interface which reduces the length over which the phase change occurs. However, after a certain value, the error starts to increase again. The results for the stabilized and non-stabilized scheme differ greatly at this point. For the case of the non-stabilized scheme, the error increase is drastic and is due to the appearance of oscillations



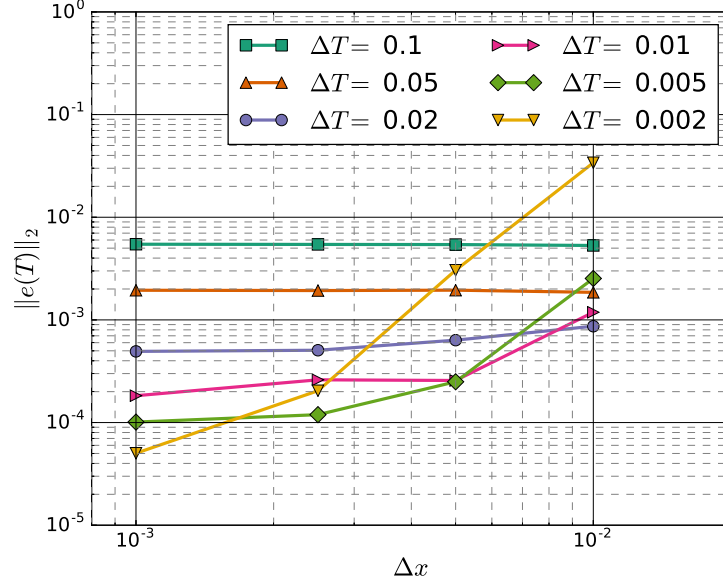


Figure 3:  $\mathcal{L}^2$  norm of the error for the Stefan problem using a standard Galerkin formulation

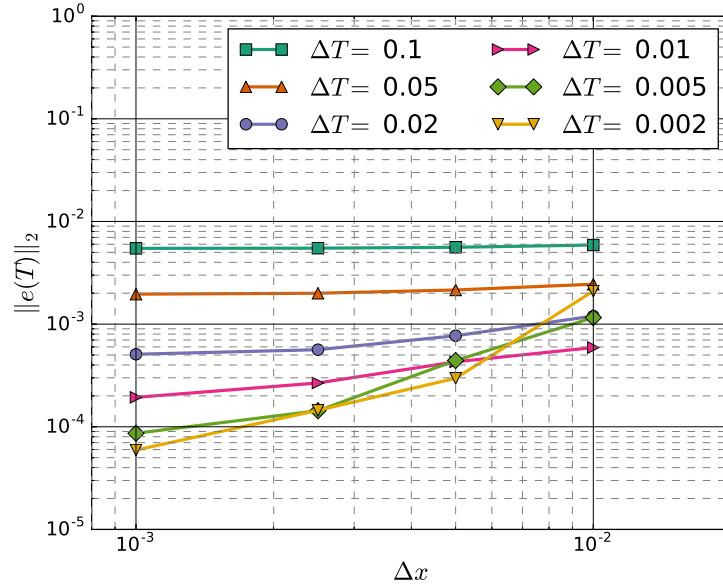


Figure 4:  $\mathcal{L}^2$  norm of the error for the Stefan problem with GGLS stabilization

in the first few time steps which lead to a violation of the positivity of the temperature. This, in turns leads to zones of negative temperature which induce significant errors over the whole domain. For the stabilized scheme, the temperature remains positive and the error remains of the same order of magnitude. It also took on average 5 times less iterations of the non-linear resolution to reach a solution with the GGLS stabilization compared to the regular Galerkin formulation.

As the mesh is refined (for lower  $\Delta x$  in Figure 3 and 4), the threshold value of  $\Delta T$  over which a minimal error is obtained is lowered since there are more nodes that be can used to represent the phase change interval. For  $\Delta x = 0.001$ , it can be clearly observed that the scheme converges to the analytical solution as the solidification interval decreases. In this case, reducing the solidification interval by a factor of 50 leads to a decrease in the norm of the error by a factor of 100.

Figure 5 shows the normalized interface thickness ( $\frac{\Delta x \Delta T}{\Delta x}$ ), which is defined as the maximal distance between two nodes which are at a value  $T_l - 0.01\Delta T$  and  $T_s + 0.01\Delta T$  when using GGLS. For the higher values of the solidification interval ( $\Delta T = 0.1$  and  $\Delta T = 0.05$ ), the relative thickness is inversely proportional to  $\Delta x$ , which means that the interface length is mesh independent. However, for the smaller intervals ( $\Delta T = 0.005$  and  $\Delta T = 0.002$ ) the relative thickness barely increases as the mesh is refined. This means that the original mesh does not contain a sufficient number of elements to accommodate the interface. It is interesting to note that the GGLS stabilization allows the interface to reside in thickness as small as two elements while ensuring the positivity of the temperature and preventing oscillations.

From our in-depth analysis of the Stefan test case, it appears that in conduction-dominated problems, the interface thickness, is a parameter that has the highest impact on the error of the solution. This has not been studied in-depth before in the literature. Furthermore, the stabilized scheme allows the use of a smaller solidification interval without generating oscillations. It preserves the positivity of the temperature which is a highly desirable property, especially for uses in

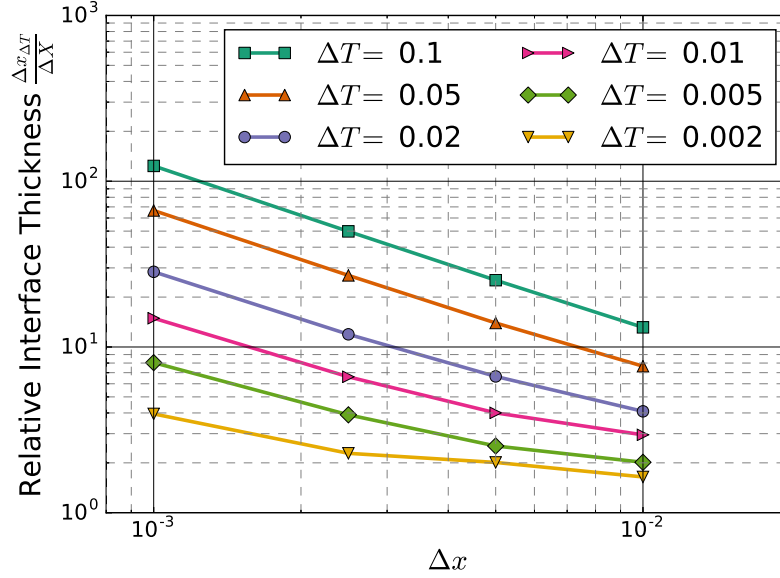


Figure 5: Relative thickness of the interface for various mesh spacing  $\Delta x$  and phase change interval  $\Delta T$ .

meshes for which the element size can vary greatly such as those required for industrial problems.

### 3.2. Natural convection between plates

A simple natural convection flow is the case of the natural convection between two infinite plates for which an analytical solution exist [26]. The configuration for this flow is illustrated at Figure 6. This test is highly representative of natural convection when there is a distinct scale separation between the geometrical dimensions of the flow, such as in the initial state of a melting cavity of reservoir. In this case, the temperate profile is independent of the velocity profile since  $H/W \gg 1$ . This results in a Couette profile for the temperature driven by conduction alone:

$$T(x) = T_L + (T_L - T_R) \frac{x}{2B} \quad (26)$$

This temperature profiles then drives the Boussinesq source term in the Navier-Stokes equation, which in turns leads to the following profile [26]

$$\mathbf{u} = [0, v(x), 0]$$

$$v(x) = \frac{\rho_0 g \beta (T_L - T_R) B_F^2}{12\mu} \left( \left( \frac{x}{B_F} \right)^3 - \left( \frac{x}{B_F} \right) \right) \quad (27)$$

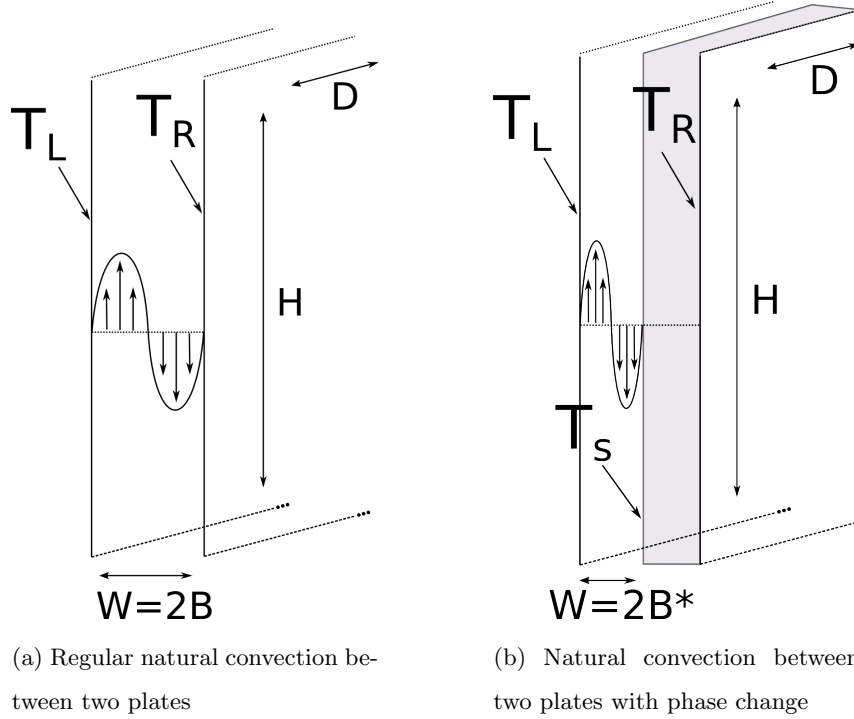


Figure 6: Natural convection between two plates. The configuration in (a) is the classical case from Bird *et al.* [26] whereas the configuration in (b) considers a solid-liquid interface and is used in the present work for verification. Both flows possess the same analytical solution (27) with a differently defined width  $B$ .

This test can easily be extended to account for phase change flow if the phase transition is set at a temperature in the interval  $[\min(T_L, T_R), \max(T_L, T_R)]$ . This has the consequence of reducing the velocity magnitude and the flow width due to the change of width of free flowing fluid domain (i.e a change of  $B$  to  $B^*$  in (27)). This configuration is illustrated in Figure 6b. The infinite plate

geometry cannot be simulated directly, but we consider the case where the ratio between the height ( $H$ ) and the width ( $2B$ ) is 100 and we monitor the velocity profile in a small region in the center of the domain ( $y \in [4.5, 5.5]$ ). Table 1 presents the parameters and the mesh characteristics of the case studied.

Table 1: Simulation parameters for the natural convection flow between plates.

|                                  |                               |
|----------------------------------|-------------------------------|
| Half-width ( $B$ )               | 0.05m                         |
| Depth                            | 0.1 m                         |
| Height ( $H$ )                   | 10m                           |
| Domain                           | $[0,0,0] \times [0.1,10,0.1]$ |
| Fluid viscosity                  | 1 Pa.s                        |
| Fluid density                    | 1 Kg/m <sup>3</sup>           |
| Coefficient of expansion $\beta$ | 1 °C <sup>-1</sup>            |
| Reynolds number                  | 0.15                          |

This test is carried out by simulating the steady flow between the plates and altering the position of the solid-liquid interface, by modifying the liquidus temperature, such that this position goes from 0.05 to 0.0498 ( $\delta x_{interface}$  from 0 to 0.002). Consequently, the interface has been displaced over a complete element ( $\frac{\delta x}{\Delta x}$  from 0 to 1). In cases where the position of the solid-liquid interface is not conformal with the mesh, the no-slip boundary condition in the solidified region is imposed using either the  $\mu$ -Penalization or the IB method. Figure 8 presents the ratio between the norm of the error when using the  $\mu$ -Penalization and the IB method ( $\frac{\|e(v)_\mu\|_2}{\|e(v)_{IB}\|_2}$ ) as a function of the displacement of the interface ( $\delta x_{interface}$ ) normalized by the spacing between the elements in the  $x$  direction ( $\Delta x$ ). For cases where the interface is aligned with the mesh, both methods have the same error. However, when the interface is moved to reside within the elements, the  $\mu$ -Penalization approach induces an additional error due to the way the no-slip boundary condition is imposed. This error is linked to the position of the discrete gauss points at which the viscous stress are calculated which alters the position of the interface on the discretized domain. Figure

7 shows the  $y$  component of the velocity for the case where the interface is located at  $x = 0.4996$  which is the case where the relative error between the approach is maximal ( $\frac{\delta x_{interface}}{\Delta x} = 0.2$ ). It can clearly be seen that the maximal velocity is underestimated and that the no-slip condition is actually applied at a significant distance away from the interface. Clearly, the IB method allows for a much more accurate resolution of the fluid velocity for cases where the mesh is non-conformal with the position of the solid-liquid interface. However, since the analytical solution is only valid for an infinite domain, rigorous error convergence analysis cannot be carried out for this flow. Hence, in the next verification case, a Taylor-Couette flow is used to carry out such an analysis.

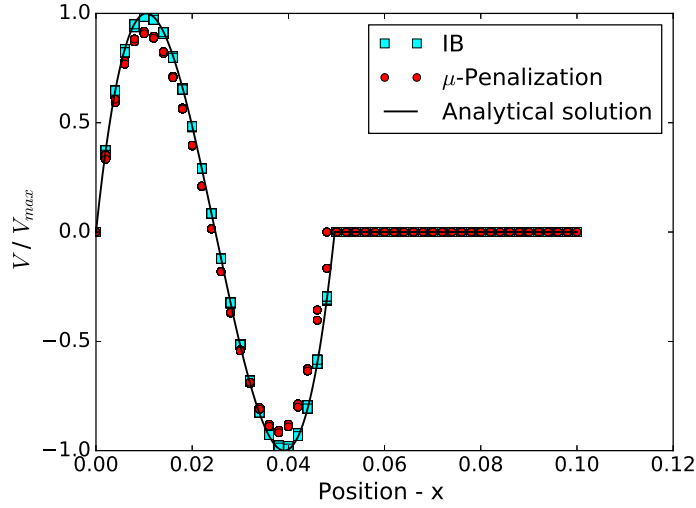


Figure 7: Axial velocity profile for the natural convection flow between two infinite plates with a solidified interface.

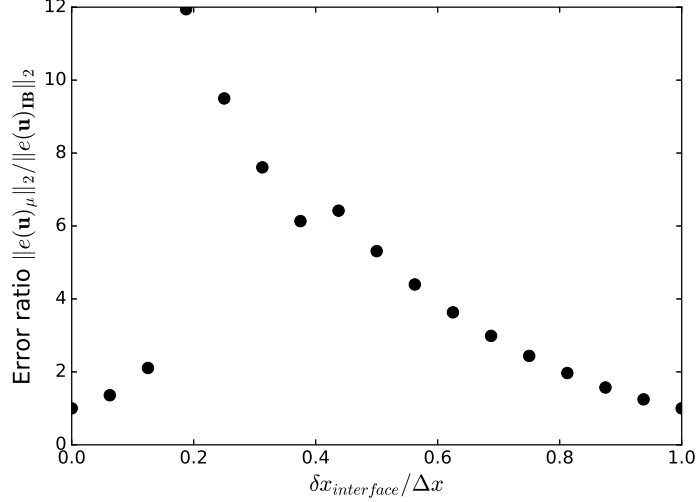


Figure 8: Relative  $\mathcal{L}^2$  norm of the error between the  $\mu$ -Penalization and the IB method. The IB method is more accurate than the  $\mu$ -Penalization when the interface is within elements.

### 3.3. Taylor-Couette flow

The second verification test case that we investigate is the well-established Taylor-Couette flow[26]. This flow, often referred to as the flow between two-concentric cylinder, is a well-established test case for methods which are designed to handle geometries which are not aligned with underlying mesh since it possesses a non-trivial analytical solution at low Reynolds number. Assuming a laminar flow, the velocity profile takes the form :

$$\mathbf{u} = [0 \ u_{\theta}(r) \ 0]^T \quad (28)$$

where  $u_{\theta}$  is the azimuthal velocity for which the analysis solution is [26]:

$$u_{\theta}(r) = \Omega \kappa R_o \left( \frac{\frac{R_o}{r} - \frac{r}{R_o}}{\frac{1}{\kappa} - \kappa} \right) \quad (29)$$

where  $r$  is the radial coordinate,  $\Omega$  is the angular velocity of the inner cylinder,  $R$  is the radius of the outer cylinder and  $\kappa$  is the ratio of the inner cylinder  $R_i$  to the outer cylinder  $R_o$  such that  $\kappa = \frac{R_i}{R_o}$ . We note that an analytical solution

also exists for the case where both the inner cylinder and the outer cylinder are rotating [26, 42].

To compare the  $\mu$ -Penalization and the IB approach, we study this flow in the three configurations illustrated in Figure 9. For the first configuration (Figure 9a), a conformal mesh is used to mesh the inner cylinder whereas the outer cylinder is imposed via the viscous penalization by imposing a jump in viscosity from the radius corresponding to the outer cylinder. In the second case (Figure 9c), the same conformal mesh is used, but the outer cylinder is imposed using the IB method. Finally, for the third configuration at Figure 9b, both the moving inner cylinder and the static outer cylinder are modeled using the IB method. These choices of configurations were made in order to ensure that the only differences in L2 norm of the error between the first and the second configuration was due to the choice of the strategy to impose no-slip on the surface of the outer cylinder. The third case is included to illustrate the capacity of the method to handle non-homogeneous Dirichlet boundary condition as well as a solid-liquid interface due to the phase transition.

Table 2 presents the dimension of the domain and the cylinders used for this case and Figure 10 illustrates the two mesh topologies used.

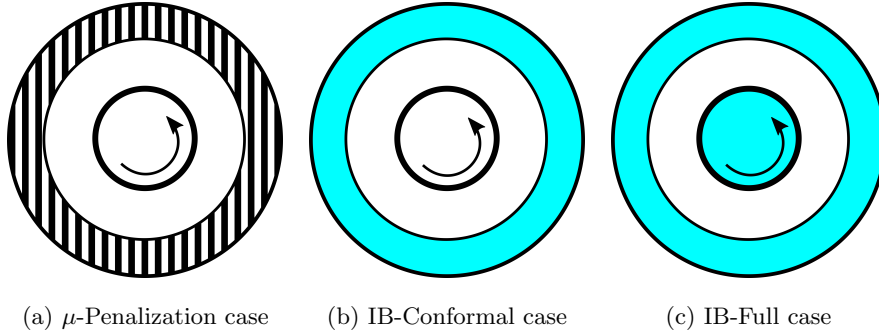


Figure 9: The three configurations used to study the Taylor-Couette flow. The shaded circles represent a cylinder over which no-slip is imposed by the viscous penalization whereas the blue-filled cylinder represents cylinders over which the IB method is used.

Figure 11 shows the evolution of the  $\|e(\mathbf{u})\|_2$  as a function of the mesh size.



Table 2: Simulation parameters for the Taylor-Couette flow

|                                    |                              |
|------------------------------------|------------------------------|
| Inner cylinder radius ( $d_p$ )    | 0.45                         |
| Outer cylinder radius ( $\rho_p$ ) | 0.15                         |
| Domain ( $\Omega$ )                | $[0, 0, 0] \times [1, 1, 1]$ |
| Reynolds number                    | 0.15                         |

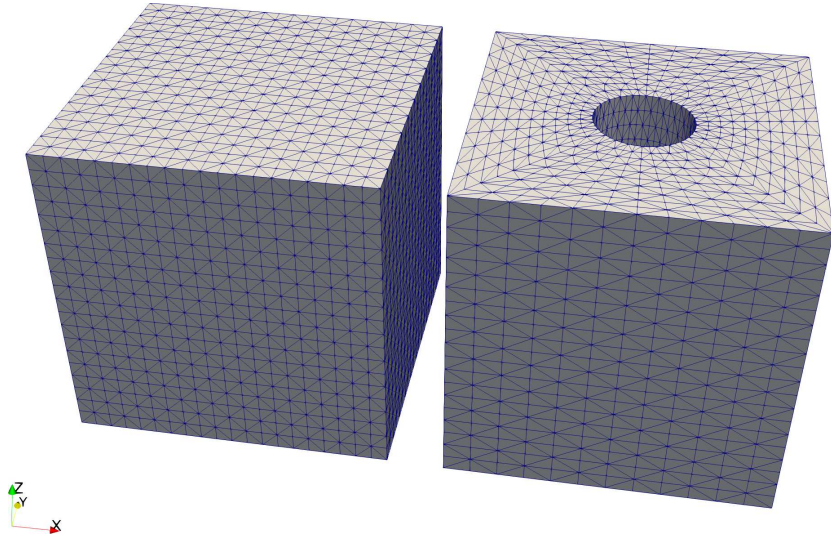


Figure 10: Mesh configurations used for the couette cases. Left : Full-IB case, Right:  $\mu$ -Penalization and IB-Conformal cases

We note that for structured P1-P1 tetrahedral GLS stabilized elements used in this work, the  $\mathcal{L}^2$  norm of the error should be such that  $\|e(\mathbf{u})\|_2 \propto \Omega_K^2$ , where  $\Omega_K$  is the characteristic size of the elements of the mesh of identical topology. For the same meshes ( $\mu$ -Penalization and IB-Conformal cases), the  $\mu$ -Penalization approach degrades the overall order of convergence of the scheme to first order whereas the IB method preserves it. Such decrease in order of convergence are often observed in penalization or other immersed boundary approach. For instance, Blais *et al.* observed a decrease to a 1.33 convergence rate for their cell-centered finite volume semi-implicit immersed boundary method.

Furthermore, for the same number of degree of freedom, the IB method always gives a lower error by a significant factor (at least  $5\times$ ). For the IB-Full case, the convergence rate is preserved, but the error constant is different from the IB-Conformal case. This difference is due to the different mesh topology used for both cases. As illustrated in Figure 10 is more adapted to the rotational symmetry of the problem. However both cases exhibit an order of convergence of 2.1.

This order of convergence is better than the theoretical order of convergence of 2. This is not an anomaly, but is due to the added DOF linked with the decomposed elements close to the IB boundary. These decomposed element add additional degree of freedom on the surface boundaries. Since these DOF are local to the decomposed elements, they are condensed at the elementary level and they are not recovered at the post-processing stage. However, they contribute to the accuracy of the solution and as such, when only the mesh DOFs are considered, the scheme exhibits better convergence. This is a nice feature to have a scheme for phase-change. Indeed, in melting cases, the accuracy of the solution close to the solid-liquid interface is critical to an accurate estimation of the interface dynamics.

We conclude that both the  $\mu$ -Penalization and IB approach lead to convergence in non-trivial flow case, but that the IB approach induces less errors and ensures that the second order  $\mathcal{L}^2$  convergence of the scheme is preserved.

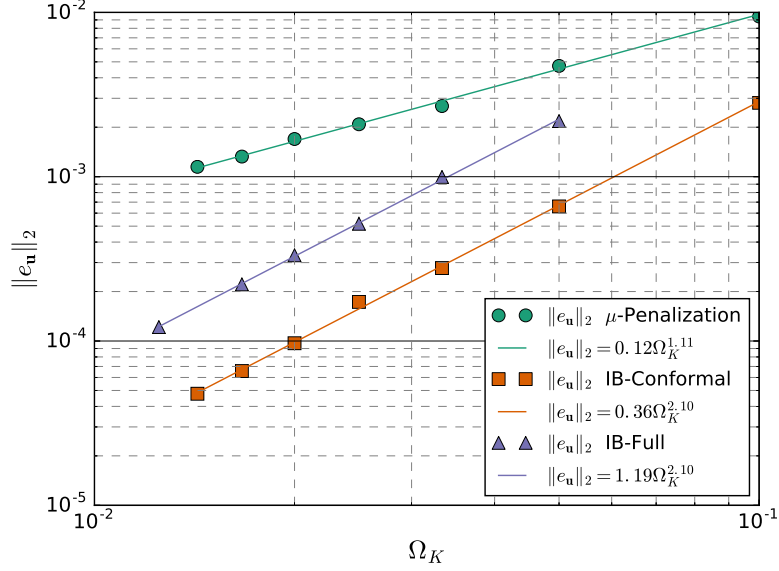


Figure 11:  $\mathcal{L}^2$  norm of the error on the velocity for the  $\mu$ -Penalization and the IB method for the configurations investigated.

#### 4. Validation: Melting cavity with natural convection

##### 4.1. Melting cavity with natural convection

The melting of metals (either tin or gallium) with natural convection within a cavity has been the benchmark for numerous numerical models for phase change and has been studied by numerous authors [4, 22, 18, 21, 43, 44, 45, 46]. It has notably been the topic of a comparison exercise [47, 17].

This case studies the melting of an initially solidified fluid within a rectangular (or prismatic in 3D) cavity which is heated by keeping one of its lateral wall at a temperature higher than the melting point. As the solid phase melts, the liquid acquires more space and natural convection becomes important. The flow structure that arise can be highly complex and multiple convection rolls can be formed depending on the value of the dimensionless number ( $St$ ,  $Ra$ ,  $Gr$ , etc.). [46]. This convection in turn, contributes to the heat transfer at the solidified interface and alters the melting rate over the height of the cavity.

Consequently, the top of the cavity melts quicker than the bottom due to the action of natural convection. At high Rayleigh number, the role of natural convection is considerable. Strong convection rolls occur and the solid at the top of the cavity melts far quicker than the bottom, leading to the formation of a distinct curved solid-liquid interface. This phenomena, which is illustrated at Figure 12, depends on the aspect ratio of the cavity ( $A = H/L$ ).

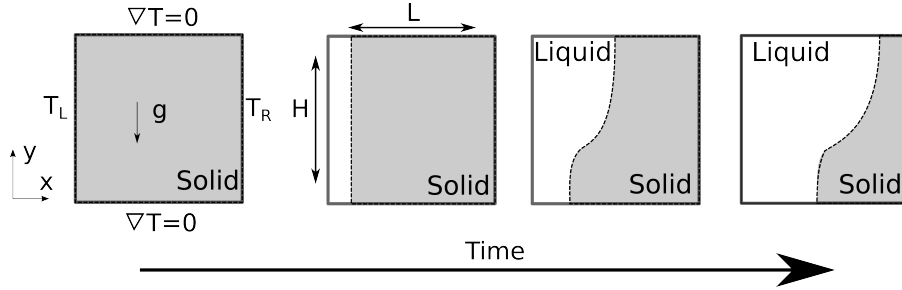


Figure 12: Illustration of the melting cavity case. Initially, the entire cavity is frozen (in grey). Then, the solid melts with a uniform front due to the action of conduction. As time progresses and the fluid occupies more space, natural convection starts to play an important role in the heat transfer and significantly alters the shape of the solid-liquid interface, leading to the formation of a curved interface.

This problem has been studied experimentally by two groups of author: Gau and Viskanta [1, 48] and Campbell *et al.* [2]. In their work [1], Gau and Viskanta studied the melting of Gallium in a three cavities of different aspect ratio ( $A = 0.714, A = 0.5, A = 0.286$ ). They measured the position of the interface at different pre-determined time by pouring out the molten metal and probing the surface of the solid interface. For the largest aspect ratio ( $A = 0.714$ ) they monitored the displacement of the interface at the top, center and bottom location. Furthermore, they measured the fraction of molten solid as a function of time. This data has been extracted from their article and will be used to validate the model in the present work.

Some authors [16] have reported that the experimental results of Gau and Viskanta are uncertain, notably when it comes to the interface position. This seems to be confirmed by the inability of Campbell *et al.* to reproduce these

results experimentally [2] or the inability of authors to reproduce them numerically [49]. However, Campbell *et al.* used a radioscopy based method to measure the interface position and this method also comes with a certain degree of uncertainty. Furthermore, some of their results implying that the interface melts quicker at the bottom than at the top appears to be non-physical.

The inability of some authors to reproduce these experiments numerically has been discussed extensively by Hannoun *et al.* [46] who highlighted the following experimental uncertainties: boundary conditions, initial conditions, metal purity and the two dimensional assumption. Indeed, since the cavity studied by Gau and Viskanta had a depth to length ratio  $D/R = D/L = 0.428$ , it unclear if the flow at high Rayleigh number might not become fully three-dimensional. Hannoun *et al.* also discussed extensively on the need for rigorous mesh-convergence analysis. Indeed, the solid-liquid interface position and the flow structures (i.e the number of rolls) were found to be dependent of numerical accuracy of the model.

In this work, we study the melting cavity in both 2D and 3D for the highest aspect ratio and Rayleigh number ( $A = 0.714$ ,  $Ra = 10^5$ ,  $Gr = 5.5 \cdot 10^6$ ,  $St_l = 0.041$ ) using the results from Gau and Viskanta [1] for the interface position, the melted fraction and the average Nusselt number. The domain used is illustrated at Figure 12. It is initially at constant temperature of  $28^\circ C$  and constant Dirichlet boundary conditions for the temperature are applied at the left (the hot wall,  $T = 38^\circ C$ ) and at the right (the cold wall,  $T = 28^\circ C$ ). Insulated boundary conditions are applied at the top and the bottom. No-slip boundary conditions are applied at the left, right, top and bottom wall. When the case is studied in  $2D$ , a thin slice is meshed and slip boundary conditions are applied in the front and back. For the  $3D$  analysis, the full prismatic cavity is meshed and no-slip boundary conditions are applied on all walls.

The liquidus temperature  $T_l$  is fixed at  $29.8^\circ C$  and the value of the solidus temperature  $T_s$  is defined via the solidification interval  $T_s = T_l - \Delta T$ . When the IB model is used, no-slip boundary condition on the solid-liquid interface is imposed at the positions where  $T = T_l$ .

Table 3 presents the cases studied as well as the mesh used. All meshes are made from structured hexahedral meshes which are then divided into tetrahedron. The number used in Table 3 denotes the number of intervals per dimension used to construct the hexahedral mesh. We note that we could not study the 3D case using the  $\mu$ -Penalization approach since the computational cost of the model was significantly (10-20x) higher than the IB model. This is linked to the difficulties in solving the linear system of equations due to the poor conditioning of the matrices caused by the high viscosity ratio required to impose stasis when the flow is dominated by convection.

To allow for an easy comparison with the results of Gau and Viskanta, all transient results are presented using the dimensionless time  $\tau = \frac{\alpha t}{L^2} \times St_l$ . Simulations presented in this work were carried out with a sufficiently small time step ( $\Delta\tau = 2 \times 10^{-5}$ ). We have found that decreasing the time step for the finer or coarser meshes considered in this work did not alter the results. However, the results are sensitive to the mesh density and a mesh convergence analysis is first carried out.

#### 4.2. Mesh independence analysis and comparison of the models

As highlighted by Hannoun *et al.* [46], the melting cavity problem can be highly sensitive to the mesh and the order of accuracy of the scheme used. We have shown in the verification cases that the IB method maintains the second order accuracy of the scheme, which is not the case for the  $\mu$ -Penalization approach. Moreover, the study of the Stefan problem shown in Section 3.1, indicated that the accuracy of the solution is dependent not only on the mesh size but also on the phase change interval  $\Delta T$ .

In this section we present the results of the effect on the solution accuracy of both the mesh and the solidification interval. Since we aim at validating the position of the solid-liquid interface, the dimensionless displacement will be used to assess the mesh independence of the solution. This dimensionless

Table 3: Simulation parameters for the Taylor-Couette flow

| Case name | Model used          | Meshes   | Viscosity Model  |
|-----------|---------------------|--|--|
| $\mu$ -2D | $\mu$ -Penalization | 80x65<br>125x100<br>187x150<br>250x200                       | Eq. (20)<br>$\mu_s = 100$<br>$\mu_l = 0.0094$<br>$n = 1.5$<br>$\phi_c = 0.6$ |
| IB-2D     | IB                  | 80x65<br>125x100<br>187x150<br>250x200<br>500x200<br>500x400 | None   |
| IB-3D     | IB                  | 125x100x20<br>125x100x40<br>187x150x40<br>225x175x60         | None   |

displacement is defined as:

$$\delta x(y) = \frac{x_{int}(y, t) - x_{int}(y, t = 0)}{L} \quad (30)$$

where  $\delta x(y)$  is the dimensionless displacement of the solid-liquid interface at a height  $y$ ,  $x_{int}(y, t)$  is the position of the interface at a time  $t$  and  $x_{int}(y, t = 0)$  the initial position of the interface.

We have found that both the position of the solid-liquid interface and the velocity profiles were the most sensitive variables to the mesh. However, the position of the interface can be easily compared over the duration of the whole simulation while the velocity profile can mostly be compared at discrete times. Analysing the former allows for an assessment of mesh independence over the entire solution.

Figure 13 shows the position of the solid-liquid interface at the Top, Center and Bottom as a function of the dimensionless time  $\tau$  for combinations of two meshes and two values of  $\Delta T$  when using the IB method. Clearly, the values of the position of the solid-liquid interface overlap for all cases considered except for the coarser meshes at the top of the cavity.

Although the problem does not possess an analytical solution, by using the finest grid (500x400) and the smallest solidification interval ( $\Delta T = 0.1$ ) we can evaluate the relative error on the position of the interface compared to the reference solution and discriminate more easily between the meshes and the values of  $\Delta T$ . The graph at Figure 14 displays the relative error on the position of the interface at the top of the cavity for the IB method. We see that the error is mostly dominated by the mesh size and not by the solidification interval.

We note that the error undergoes a sharp change for all meshes close to  $\tau = 0.35$ , which is the point at which the top interface position undergoes a slope transition as can be seen at Figure 13. Finally, meshes equal or finer than 250x200 all exhibit, for  $\tau > 0.01$ , a relative error on the interface displacement which is consistently below 2%. As such, we consider that IB results for these meshes are mesh-independent. We note that a similar mesh-sensitivity analysis, not shown here, was carried out in 3D and yielded similar results.



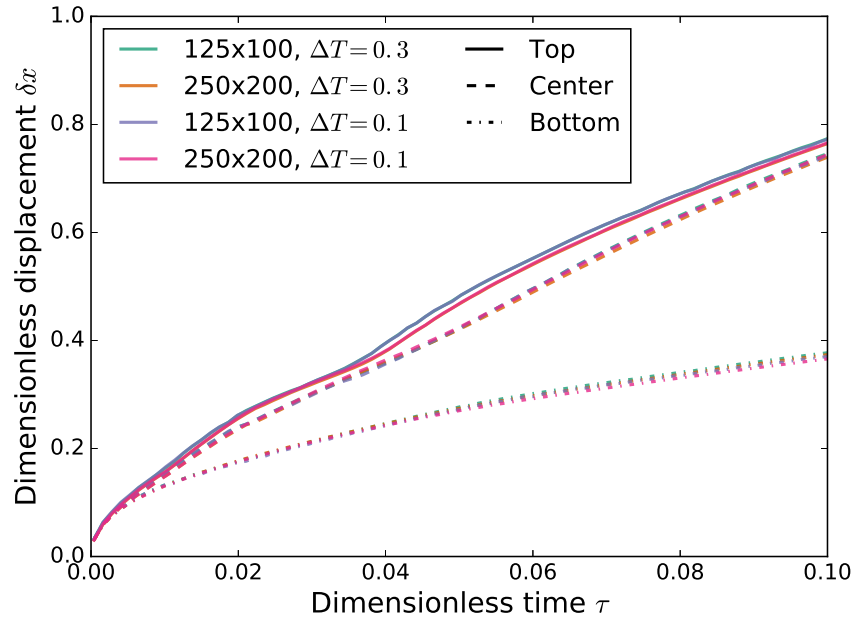


Figure 13: Comparison of the position of the solid-liquid interface at the Top (solid line), Center (dashed line) and Bottom (dotted line) for two meshes (125x100 and 250x200) and two values of the phase change interval ( $\Delta T = 0.3$  and  $\Delta T = 0.1$ ).

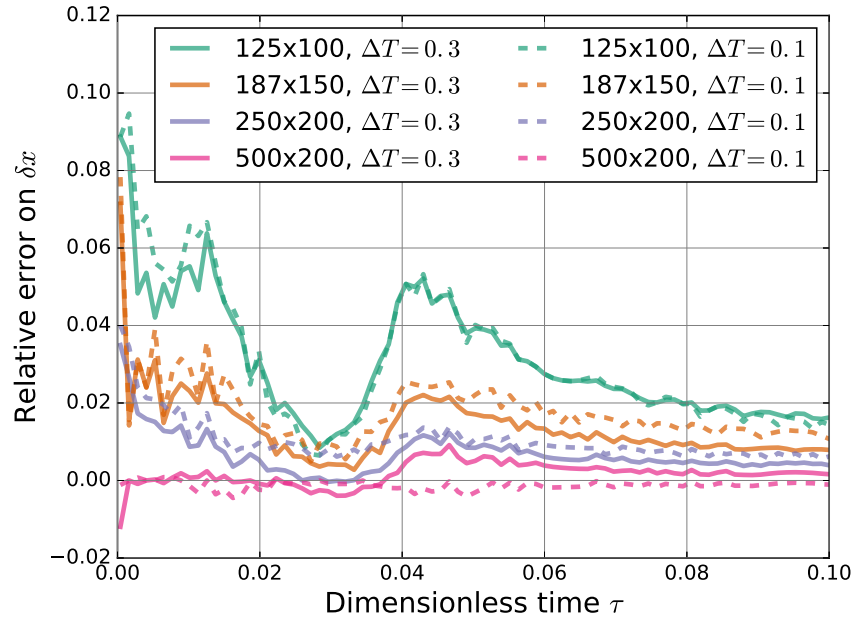


Figure 14: Relative error on the interface displacement for the IB method with respect to the finer mesh (500x400) and the smallest value of the solidification interval ( $\Delta T = 0.1$ ).

The graph at Figure 15 displays the relative error on the position of the interface at the top of the cavity for the  $\mu$ -Penalization method. In this case, the reference solution is taken for the 250x200 mesh with  $\Delta T = 0.1$ . Because of the high computational cost and the need for a sharp viscosity difference between the solid and liquid, generating a reference solution on the 500x400 mesh would have been required a needlessly high computational time. Results shown in Figure 15 indicate that the error is more affected by the value of the solidification interval  $\Delta T$  than the mesh size. Indeed, the relative error remains very small for all meshes when  $\Delta T = 0.1$ , but can be significantly larger (and non-monotonic) when solutions for  $\Delta T = 0.3$  are compared to those for  $\Delta T = 0.1$ .

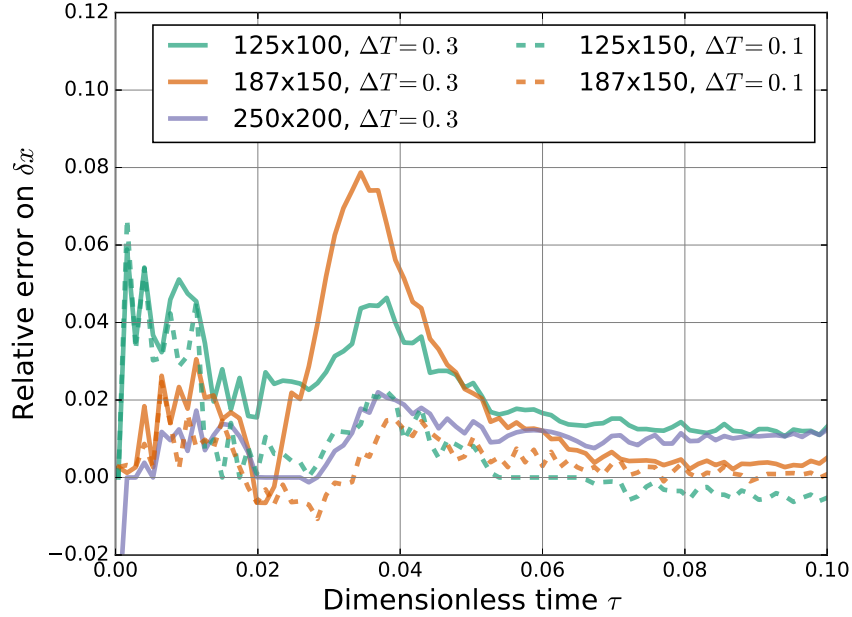


Figure 15: Relative error on the interface displacement for the  $\mu$ -Penalization method with respect to the finer mesh (250x200) and the smallest value of the solidification interval ( $\Delta T = 0.1$ ).

Figure 16 compares the two proposed methods for the 250x200 mesh with

$\Delta T = 0.1$ . Results are closer to each other for the center and the bottom locations, but the  $\mu$ -Penalization predicts slightly faster melting at the top. This is in part due to the rheological law which allows for a partial advection of the mushy zones at low solid fraction. We note that reproducing a rheological law for partially solidified fluid is also possible with the IB method, but introducing such a model should be physically justified.

As  $\Delta T \rightarrow 0$  and as the mesh is refined, this difference is expected to decrease, but even for the configurations at Figure 16 the relative difference between the two results is smaller than 3%. Consequently, in the following sections, only the results from the IB method will be considered.

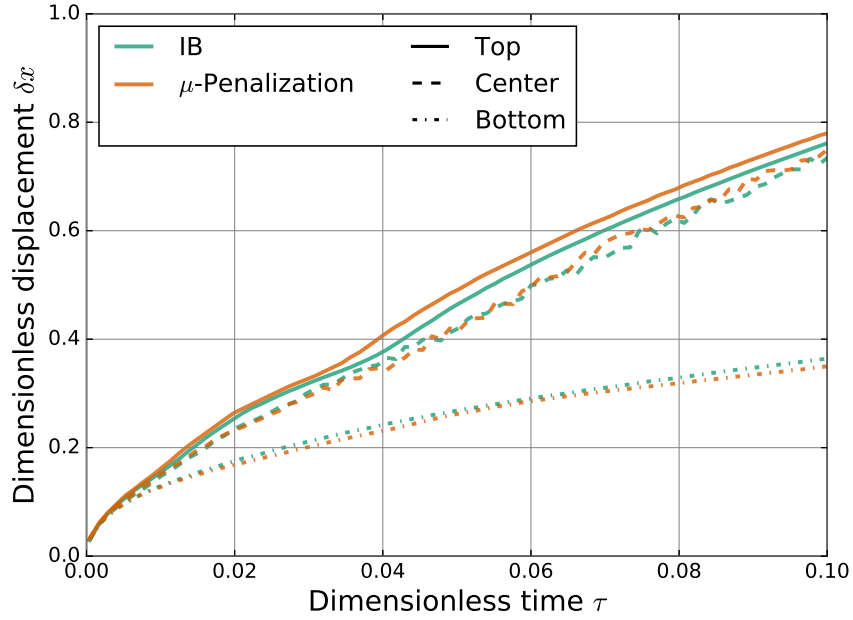


Figure 16: Comparison of the position of the solid-liquid interface at the Top (solid line), Center (dashed line) and Bottom (dotted lined) for the IB and  $\mu$ -Penalization approach for the  $250 \times 200$  mesh with  $\Delta T = 0.1$ .

#### 4.3. Validation of the interface position in 2D

The graph at Figure 17 compares the results for the position of the interface with the experimental results from Gau and Viskanta [1]. We note that the band around the lines is made of three curve corresponding to  $T = T_s + 0.01\Delta T$ ,  $T = \frac{T_l - T_s}{2}$  and  $T = T_s + 0.99\Delta T$ . The fill between the lines therefore represents 98% of the width of the phase change interval. The numerical model captures quite well the position of the interface at the bottom and at the center, but under predicts the melting at the top of the cavity for larger time ( $\tau > 0.03$ ). Although it underestimates the melting rate, the numerical solution exhibits similar feature such as a change of slope which occurs for  $\tau = 0.03$  in the experiments and  $\tau = 0.04$  in the model. It remains unclear why only the prediction of the top interface is poor, but this could be partially explained by experimental uncertainties surrounding the work of Gau and Viskanta [1] linked to the use of the pour out method, the probing of the interface and the boundary conditions.

An hypothesis put forward by Hannoun *et al.* [46] was that the flow might actually become fully 3D as the melting of the solid progresses. Considering the ratio between the cavity depth and length considered in the study by Gau ( $C = D/L = 0.429$ ) this could indeed occur. Thus we now study the same flow but using full 3D simulations.

#### 4.4. Validation of the interface position in 3D

Since all 2D simulations were actually carried out on a 3D slice, extending the analysis to a full 3D analysis is an easy endeavour. The graph at Figure 18 shows the position of the solid-liquid interface for the 3D results when using the structured 225x175x60 mesh. When comparing to the result at Figure 17, the results for the center and the top position of the interface are indeed affected by the transition to 3D. First, the two curves are much further apart than in the 2D case. Secondly, the top interface results are closer to the experimental results, at least for  $\tau < 0.4$ . Still, the model underestimates the melting at the

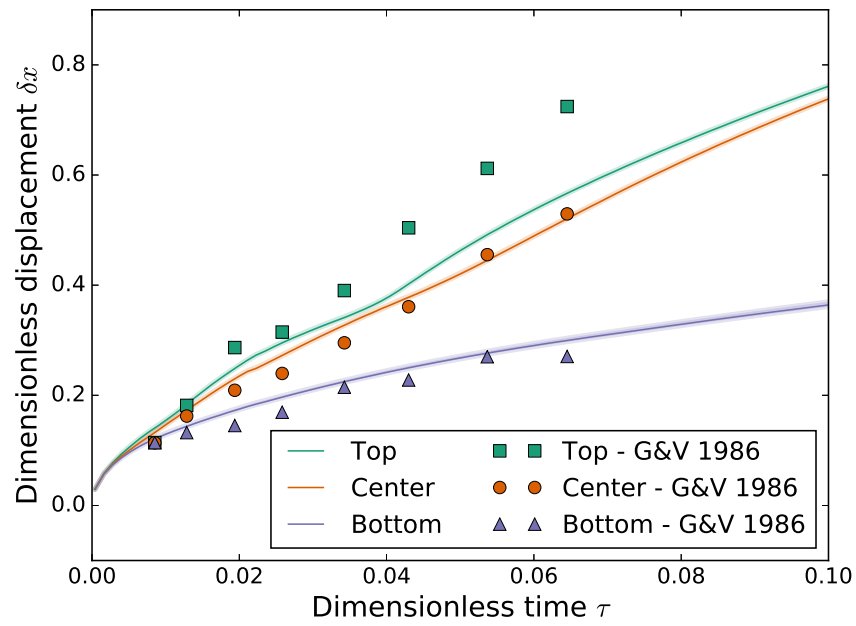


Figure 17: Comparison of the simulation results for the position of the solid-liquid interface at the top, center and bottom of the cavity with the results obtained by Gau and Viskanta [1].

top, and furthermore, underestimates the melting at the center, which was not the case for the 2D model.

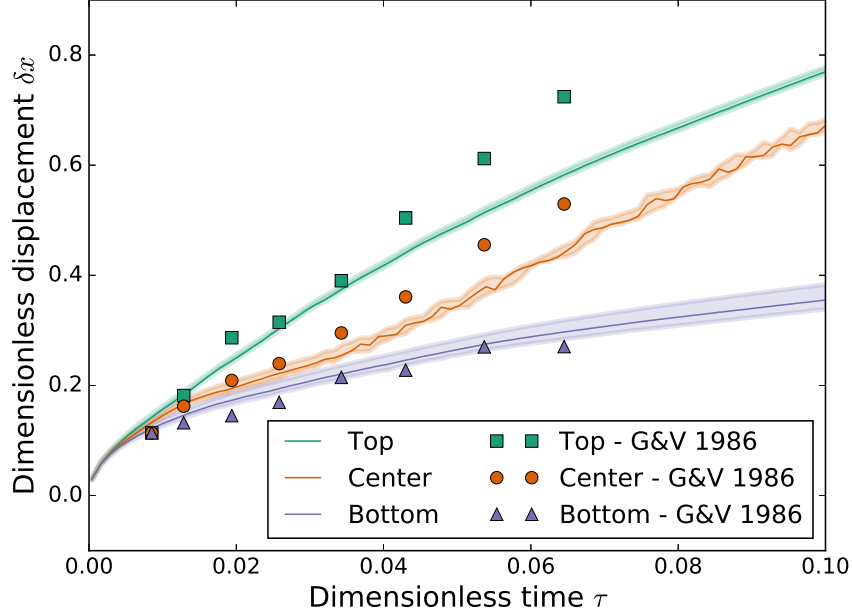


Figure 18: Comparison of the 3D simulation results for the position of the solid-liquid interface at the top, center and bottom of the cavity with the results obtained by Gau and Viskanta [1]. The tetrahedral mesh is made from 225x175x60 hexahedra decomposed in 5 tetrahedra each and the solidification interval is fixed to  $\Delta T = 0.3$ .

The flow pattern, not shown here, are altered when going from 2D to 3D. After some time ( $\tau > 0.02$ ) velocity in the  $Z$  axis (depth) becomes a significant component (approx. 20%) of the velocity magnitude. The flow circulating close to the top actually moves significantly in the  $Z$  direction and thus spends more time closer to the solidified fluid before going down. This could explain the larger difference between the top and the center interface position which occurs in the 3D model. For both the 2D and 3D analysis, it appears that the agreement with experimental results is satisfactory, but that predicting the measured position of the top interface remains challenging. The important changes in flow pattern and interface position that occur when transitioning from 2D to 3D are highly

interesting and have never been isolated before. Although they lead to a more distinct difference between the top and center interface position, they do not lead to a better agreement with the experiments.

#### 4.5. *Melted fraction*

The melted fraction is, from an engineering point of view, a highly important information. We have found that the melted volume is less sensitive to the mesh, the phase change interval  $\Delta T$  and the dimensionality of the problem than the interface position. Figure 19 presents the fraction of melted volume for the 2D and 3D analysis as well as the data extracted from Gau and Viskanta [1]. Both results agree well with the experimental results of Gau and Viskanta, but the 3D models predicts a slightly lower melted fraction at longer time. This may be attributable to the flow hindering that occur due to the front and back wall, which in turn reduces the action of convection and lowers the melting speed. Overall, the agreement between the simulations and the experiment is good.

#### 4.6. *Nusselt number*

The average Nusselt number is a good metric to quantify the role of convection in the thawing process within the melting cavity. It can easily be obtained from simulation results by calculating the temperature gradient normal to the hot wall. Obtaining it experimentally is a more complex endeavour. Gau and Viskanta measure the average Nusselt number experimentally using the fraction of melted solid which was measured via a pour out method. This actually, as noted by the authors, measures a time-averaged Nusselt number. We note that the  $X$  axis of the graph from Gau and Viskanta appears to be erroneously labelled (the values are 10x too small), otherwise the Nusselt results and the time at which they are calculated do not match that of any of the other figures and would correspond to a melting that would have occurred in 2 minutes instead of the 20 minutes reported throughout the paper.

The graph at Figure 20 shows the average Nusselt  $Nu_A$  number on the hot wall as a function of the dimensionless time  $\tau$  for both the 2D and the 3D



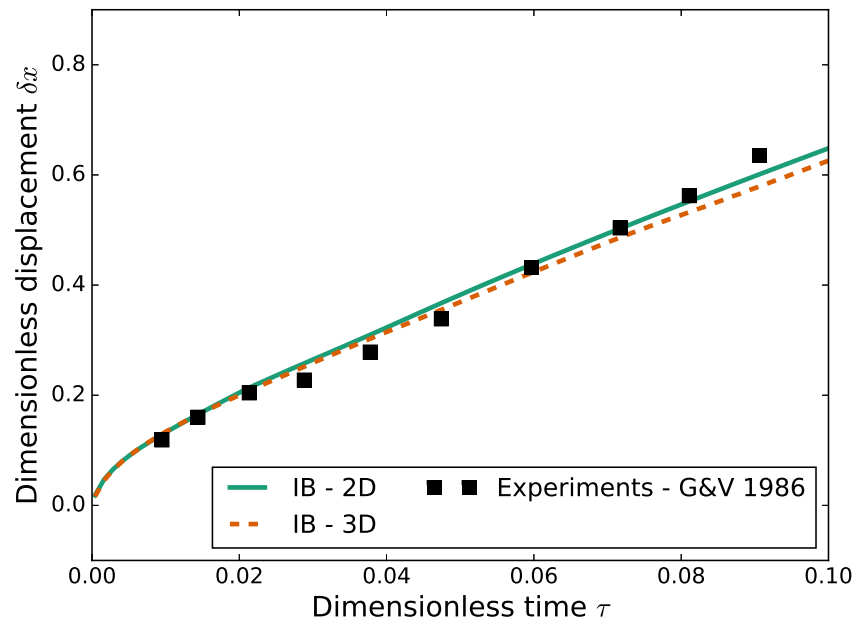


Figure 19: Comparison of the melted volume for the 2D and 3D simulations with the results obtained by Gau and Viskanta [1].

model. For all models,  $Nu_A$  is initially very large, due to the strong action of conduction, and then levels off to a constant value due to the convection that takes place within the cavity. In the  $2D$  case,  $Nu_A$  undergoes a drastic change at  $\tau = 0.02$ . The graph at Figure 21 shows the local Nusselt profile along the hot wall of the cavity for the  $2D$  model. It can be seen that for  $\tau < 0.02$ , the local Nusselt number has three peaks which are associated with three vortices. For  $\tau > 0.02$ , the number of vortices is reduced to two and at longer time ( $\tau > 0.06$ ) only a single vortex remains. This change in the number of vortices significantly alters the heat transfer at the wall.

For the  $3D$  model, the flow structure appear to be a lot more stable. Consequently, the average Nusselt number  $Nu_A$  decreases quasi-monotonically and level off at a value much closer to the experimental results. Furthermore, although some slight oscillations appear in  $Nu_A$ , they are at a much lower frequency. These results highlight the difference between the solutions reported in Sections 4.3 and 4.4.

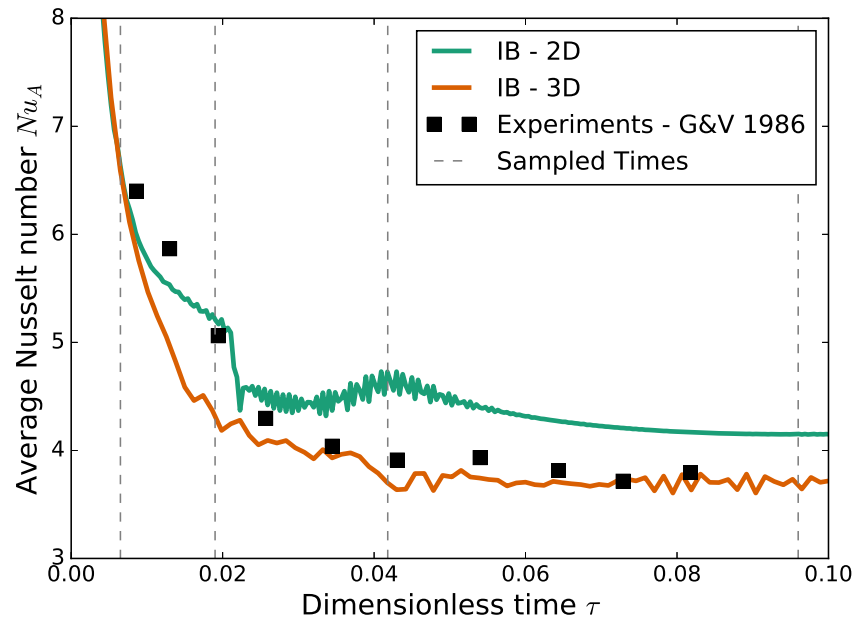


Figure 20: Comparison of the space-averaged Nusselt number at the hot wall with the results obtained by Gau and Viskanta [1].

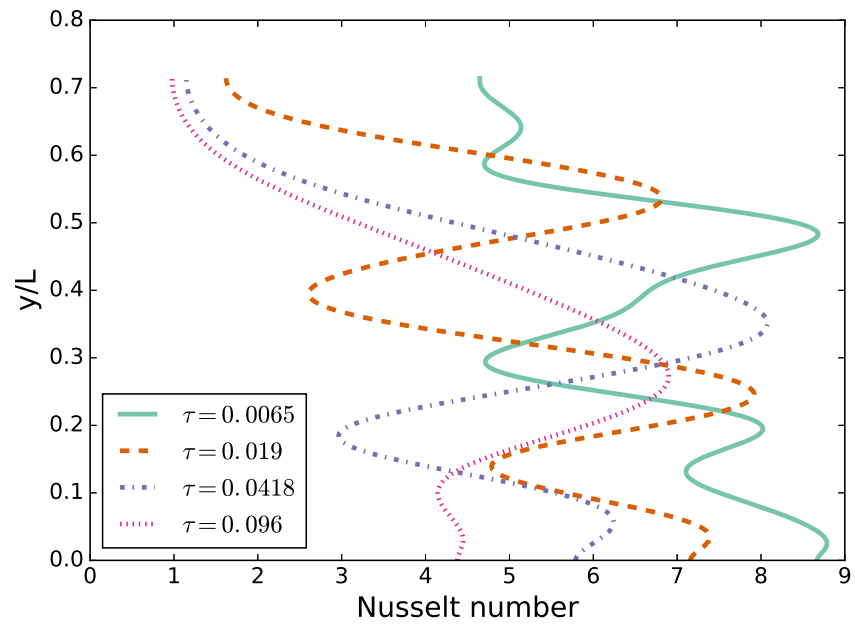


Figure 21: Local Nusselt number on the hot wall of the cavity at four distinctive moments.

## 5. Conclusion

The modelling of solidification and melting is a challenging topic due to the strong coupling between the Navier-Stokes and energy equations as well as the stiff non-linear dependence of the physical properties on the temperature. In this work, we have presented two stabilized finite element models to accurately solve phase change problems with natural convection.

The first model ( $\mu$ -Penalization) uses a viscosity penalization to impose stasis in the solidified region whereas the second model (IB) uses an immersed boundary method to impose this stasis.

By our in depth analysis of the Stefan problem we have shown that the accuracy of the scheme can be controlled not only by the mesh size, but also by the choice of the solidification interval. Indeed, for conduction dominated problems, this parameter can have a greater influence on the error than the mesh size.

By analysing the natural convection between two infinite plates, we have demonstrated that the IB method can resolve the flow with greater accuracy when the solid-liquid interval lies inside elements, something which occurs naturally in phase change problems. By studying the Taylor-Couette flow, we have demonstrated that the IB approach consistently gives smaller error and preserves the second order of convergence of the  $\mathcal{L}^2$  norm of the error whereas the  $\mu$ -Penalization reduced the scheme to a first order one.

The two models were finally used to shed light on the melting within a rectangular cavity. After having demonstrated mesh convergence, we have shown that both the IB and  $\mu$ -Penalization method gave similar results. These results showed good agreement with the experiments of Gau and Viskanta for the center and bottom position of the interface, but under-predicted the melting at the top of the cavity. Simulations in 3D were then carried out to evaluate if the dimensionality of the problem was leading to this under-prediction. To the best of our knowledge, these simulations were the first of their kind. The 3D results were significantly different from the 2D results. They lead to a larger melting

rate at the top which, while it lead to a better agreement with the experiments, was still an under-prediction. However, the *3D* results also showed less melting in the center, which lead to a disagreement with both the experimental and *2D* results. Yet, the overall behaviour of the *3D* results and the stronger distinction between the center and the top melted position appeared in better agreement with the experimental results overall.

The *2D* and *3D* model were also found to be able to predict accurately the melted fraction of solid, with the *3D* model slightly under-predicting this fraction at larger time. Finally, significant differences were observed between the *2D* and the *3D* model for the prediction of the evolution of the average Nusselt number. The average Nusselt number predicted by the *2D* model was found to be much higher at lower time and presented a sharp change after a certain time ( $\tau \approx 0.02$ ) which was associated to a change from a 3 vortices to 2 vortices flow pattern. The *3D* model presented a much smoother profile without any sudden change and exhibited very good agreement to the experimental results, especially at longer time. These results have highlighted the need for accurate and robust CFD model which can take into account the phase change in complex three-dimensional geometries since even simple geometries can be affected by *3D* phenomena.

This work opens possibilities for numerous topics related to solidification and melting. In future work, the method developed in this work will be extended to free surface flows to study how changes in density during solidification affect the position of the free surface. Furthermore, the stresses arising from the solidification of an expanding liquid, such as AdBlue, will be studied via a complete fluid-structure interaction model.

## 6. Acknowledgements

The authors wish to thank the Energy Innovation Program of the Office for Energy Research and Development (Natural Resources Canada) and the Advanced Manufacturing Program of the National Research Council Canada

for their financial support. The first author would also like to acknowledge Dr. Kintak Yu for fruitful discussions and for his input on the validation procedure.

## References

- [1] C. Gau, R. Viskanta, Melting and solidification of a pure metal on a vertical wall 108 (1) 174–181. doi:10.1115/1.3246884.  
URL <http://dx.doi.org/10.1115/1.3246884>
- [2] T. A. Campbell, J. N. Koster, Visualization of liquid-solid interface morphologies in gallium subject to natural convection 140 (3) 414–425. doi:10.1016/0022-0248(94)90318-2.  
URL <http://www.sciencedirect.com/science/article/pii/0022024894903182>
- [3] R. Viswanath, Y. Jaluria, A comparison of different solution methodologies for melting and solidification problems in enclosures, Numerical Heat Transfer, Part B Fundamentals 24 (1) (1993) 77–105.
- [4] R. Viswanath, Y. Jaluria, Numerical study of conjugate transient solidification in an enclosed region, Numerical Heat Transfer, Part A: Applications 27 (5) (1995) 519–536.
- [5] A. A. Al-abidi, S. Bin Mat, K. Sopian, M. Y. Sulaiman, A. T. Mohammed, CFD applications for latent heat thermal energy storage: a review 20 353–363. doi:10.1016/j.rser.2012.11.079.  
URL <http://www.sciencedirect.com/science/article/pii/S1364032112006934>
- [6] N. H. S. Tay, F. Bruno, M. Belusko, Experimental validation of a CFD model for tubes in a phase change thermal energy storage system 55 (4) 574–585. doi:10.1016/j.ijheatmasstransfer.2011.10.054.  
URL <http://www.sciencedirect.com/science/article/pii/S001793101100634X>

- [7] A. Trp, An experimental and numerical investigation of heat transfer during technical grade paraffin melting and solidification in a shell-and-tube latent thermal energy storage unit 79 (6) 648–660. doi:10.1016/j.solener.2005.03.006.  
URL <http://www.sciencedirect.com/science/article/pii/S0038092X05001337>
- [8] Y. Dutil, D. R. Rousse, N. B. Salah, S. Lassue, L. Zalewski, A review on phase-change materials: Mathematical modeling and simulations 15 (1) 112–130. doi:10.1016/j.rser.2010.06.011.  
URL <http://www.sciencedirect.com/science/article/pii/S1364032110001589>
- [9] E. Assis, L. Katsman, G. Ziskind, R. Letan, Numerical and experimental study of melting in a spherical shell 50 (9) 1790–1804. doi:10.1016/j.ijheatmasstransfer.2006.10.007.  
URL <http://www.sciencedirect.com/science/article/pii/S0017931006005503>
- [10] I. W. Eames, K. T. Adref, Freezing and melting of water in spherical enclosures of the type used in thermal (ice) storage systems 22 (7) 733–745. doi:10.1016/S1359-4311(02)00026-1.  
URL <http://www.sciencedirect.com/science/article/pii/S1359431102000261>
- [11] S. aus der Wiesche, Numerical heat transfer and thermal engineering of AdBlue (SCR) tanks for combustion engine emission reduction 27 (11) 1790–1798. doi:10.1016/j.applthermaleng.2007.01.008.  
URL <http://www.sciencedirect.com/science/article/pii/S1359431107000373>
- [12] B. Choi, S.-M. Woo, Numerical analysis of the optimum heating pipe to melt frozen urea-water-solution of a diesel urea-scr system, Applied Thermal Engineering 89 (2015) 860–870.



- [13] B.-C. Choi, Y. K. Kim, W.-N. Jhung, C.-H. Lee, C.-Y. Hwang, Experimental investigation on melting characteristics of frozen ureawater-solutions for a diesel SCR de-NOx-system 50 (1) 1235–1245. doi:10.1016/j.applthermaleng.2012.08.008.  
URL <http://www.sciencedirect.com/science/article/pii/S1359431112005303>
- [14] S. A. Khairallah, A. T. Anderson, A. Rubenchik, W. E. King, Laser powder-bed fusion additive manufacturing: Physics of complex melt flow and formation mechanisms of pores, spatter, and denudation zones 108 36–45. doi:10.1016/j.actamat.2016.02.014.  
URL <https://www.sciencedirect.com/science/article/pii/S135964541630088X>
- [15] F. J. Grtler, M. Karg, K. H. Leitz, M. Schmidt, Simulation of laser beam melting of steel powders using the three-dimensional volume of fluid method 41 881–886. doi:10.1016/j.phpro.2013.03.162.  
URL <http://www.sciencedirect.com/science/article/pii/S1875389213001764>
- [16] H. Udaykumar, W. Shyy, M. Rao, Elafint-a mixed eulerian-lagrangian method for fluid flows with complex and moving boundaries, in: 6th Joint Thermophysics and Heat Transfer Conference, 1996, p. 1996.
- [17] O. Bertrand, B. Binet, H. Combeau, S. Couturier, Y. Delannoy, D. Gobin, M. Lacroix, P. Le Qur, M. Mdale, J. Mencinger, H. Sadat, G. Vieira, Melting driven by natural convection a comparison exercise: first results 38 (1) 5–26. doi:10.1016/S0035-3159(99)80013-0.  
URL <http://www.sciencedirect.com/science/article/pii/S0035315999800130>
- [18] P. Nithiarasu, An adaptive finite element procedure for solidification problems 36 (3) 223–229. doi:10.1007/s002310050389.  
URL <http://link.springer.com/article/10.1007/s002310050389>

- [19] P. Angot, C.-H. Bruneau, P. Fabrie, A penalization method to take into account obstacles in incompressible viscous flows 81 (4) 497–520. doi:10.1007/s002110050401.  
URL <https://link.springer.com/article/10.1007/s002110050401>
- [20] B. Blais, M. Lassaigne, C. Goniva, L. Fradette, F. Bertrand, A semi-implicit immersed boundary method and its application to viscous mixing 85 136–146. doi:10.1016/j.compchemeng.2015.10.019.  
URL <http://www.sciencedirect.com/science/article/pii/S0098135415003488>
- [21] J. Mencinger, Numerical simulation of melting in two-dimensional cavity using adaptive grid 198 (1) 243–264. doi:10.1016/j.jcp.2004.01.006.  
URL <http://www.sciencedirect.com/science/article/pii/S0021999104000269>
- [22] C. Huber, A. Parmigiani, B. Chopard, M. Manga, O. Bachmann, Lattice boltzmann model for melting with natural convection 29 (5) 1469–1480. doi:10.1016/j.ijheatfluidflow.2008.05.002.  
URL <http://www.sciencedirect.com/science/article/pii/S0142727X08000957>
- [23] E. A. Semma, M. El Ganaoui, R. Bennacer, Lattice boltzmann method for melting/solidification problems 335 (5) 295–303. doi:10.1016/j.crme.2007.05.015.  
URL <http://www.sciencedirect.com/science/article/pii/S163107210700085X>
- [24] E. Semma, M. El Ganaoui, R. Bennacer, A. A. Mohamad, Investigation of flows in solidification by using the lattice boltzmann method 47 (3) 201–208. doi:10.1016/j.ijthermalsci.2007.02.010.  
URL <http://www.sciencedirect.com/science/article/pii/S1290072907000695>

- [25] W. Ogoh, D. Groulx, Stefans problem: Validation of a one-dimensional solid-liquid phase change heat transfer process, in: Comsol Conference 2010, 2010.
- [26] R. B. Bird, Transport phenomena, Applied Mechanics Reviews 55 (1) (2002) R1–R4.
- [27] T. E. Tezduyar, R. Shih, S. Mittal, R. S. E, Incompressible flow using stabilized bilinear and linear equal-order-interpolation velocity-pressure elements, Research Report UMSI 90/165.
- [28] F. Ilinca, D. Pelletier, A. Garon, An adaptive finite element method for a two-equation turbulence model in wall-bounded flows, International Journal for Numerical Methods in Fluids 24 (1997) 101–120.
- [29] L. P. Franca, S. L. Frey, Stabilized finite element methods: Ii. the incompressible navier-stokes equations, Computer Methods in Applied Mechanics and Engineering 99 (2-3) (1992) 209–233.
- [30] L. P. Franca, E. G. Dutra Do Carmo, The galerkin gradient least-squares method, Computer Methods in Applied Mechanics and Engineering 74 (1989) 41–54.
- [31] F. Ilinca, J.-F. Héту, Three-dimensional finite element solution of the flow in single and twin-screw extruders 25 (4) 275–286. doi:10.3139/217.2351. URL <http://www.hanser-elibrary.com/doi/abs/10.3139/217.2351>
- [32] F. Ilinca, J. F. Héту, A finite element immersed boundary method for fluid flow around moving objects 39 (9) 1656–1671. doi:10.1016/j.compfluid.2010.06.002. URL <http://www.sciencedirect.com/science/article/pii/S0045793010001337>
- [33] F. Ilinca, J.-F. Héту, A finite element immersed boundary method for fluid flow around rigid objects 65 (7) 856–875. doi:10.1002/fluid.2222.

URL <http://onlinelibrary.wiley.com/doi/10.1002/fld.2222/abstract>

- [34] F. Ilinca, J.-F. Héту, Solution of flow around complex-shaped surfaces by an immersed boundary-body conformal enrichment method 69 (4) 824–841. doi:10.1002/fld.2615.

URL <http://onlinelibrary.wiley.com/doi/10.1002/fld.2615/abstract>

- [35] J. F. Héту, F. Ilinca, Immersed boundary finite elements for 3d flow simulations in twin-screw extruders 87 2–11. doi:10.1016/j.compfluid.2012.06.025.

URL <http://www.sciencedirect.com/science/article/pii/S0045793012002484>

- [36] F. Ilinca, J.-F. Héту, An immersed boundary-body conformal enrichment method for thermal flow problems, Computers & Fluids 88 (2013) 616–628.

- [37] F. Ilinca, J.-F. Héту, Immersed boundary solution of natural convection in a square cavity with an enclosed rosette-shaped hot cylinder, Numerical Heat Transfer, Part A: Applications 65 (12) (2014) 1154–1175.

- [38] W. L. Oberkampf, T. G. Trucano, Verification and validation in computational fluid dynamics, Progress in Aerospace Sciences 38 (3) (2002) 209–272.

- [39] P. J. Roache, Verification and validation in computational science and engineering, Vol. 895, Hermosa Albuquerque, NM, 1998.

- [40] B. Blais, F. Bertrand, On the use of the method of manufactured solutions for the verification of CFD codes for the volume-averaged navierstokes equations 114 121–129. doi:10.1016/j.compfluid.2015.03.002.

URL <http://www.sciencedirect.com/science/article/pii/S0045793015000675>

- [41] E. Jones, T. Oliphant, P. Peterson, et al., SciPy: Open source scientific tools for Python (2001–).  
URL <http://www.scipy.org/>
- [42] S. Chandrasekhar, Hydrodynamic and hydromagnetic stability, Courier Corporation, 2013.
- [43] M. A. Cruchaga, D. J. Celentano, A fixed-mesh finite element thermally coupled flow formulation for the numerical analysis of melting processes, *International Journal for Numerical Methods in Engineering* 51 (10) (2001) 1231–1258.
- [44] D. J. McDaniel, N. Zabaras, A least-squares front-tracking finite element method analysis of phase change with natural convection, *International Journal for Numerical Methods in Engineering* 37 (16) (1994) 2755–2777.
- [45] C. Desai, K. Vafai, A unified examination of the melting process within a two-dimensional rectangular cavity, *Journal of heat transfer* 115 (4) (1993) 1072–1075.
- [46] N. Hannoun, V. Alexiades, T. Z. Mai, Resolving the controversy over tin and gallium melting in a rectangular cavity heated from the side, *Numerical Heat Transfer: Part B: Fundamentals* 44 (3) (2003) 253–276.
- [47] D. Gobin, P. Le Quéré, Melting from an isothermal vertical wall. synthesis of a numerical comparison exercise, *Computer Assisted Mechanics and Engineering Sciences* 7 (3) (2000) 289–306.
- [48] C. Gau, R. Viskanta, Melting and solidification of a metal system in a rectangular cavity, *International Journal of Heat and Mass Transfer* 27 (1) (1984) 113–123.
- [49] M. Lacroix, V. Voller, Finite difference solutions of solidification phase change problems: transformed versus fixed grids, *Numerical Heat Transfer* 17 (1) (1990) 25–41.